applied system innovation

MDPI

*Article*

# Optimizing Peltier Cooling Performance in Hot Environments: A Comparative Study of Python Empirical Modeling and MATLAB Simulink

**Miguel Antonio Domínguez-Crespo, Aidé Minerva Torres-Huerta, Héctor Yahir Álvarez-Olvera, Aida Medina-González and Facundo Joaquín Márquez-Rocha ***

Unidad Profesional Interdisciplinaria de Ingeniería, Campus Hidalgo, Instituto Politécnico Nacional, DESCTI, San Agustín Tlaxiaca 42162, Hidalgo, Mexico; mdominguezc@ipn.mx (M.A.D.-C.); atorresh@ipn.mx (A.M.T.-H.); halvarezo2100@alumno.ipn.mx (H.Y.Á.-O.); amedinago@ipn.mx (A.M.-G.)
* Correspondence: fmarquez@ipn.mx

## Abstract

This study presents a comparative analysis of the energy and thermal behavior of a Peltier module operating in hot environments (28 °C to 40 °C) using Python and MATLAB/Simulink. A theoretical block model was developed to define governing equations, while an empirical Python-based framework was implemented to capture real-world non-linearities. Results demonstrate that heat absorption is fundamentally dependent on efficient heat dissipation; a maximum coefficient of performance (COP) of 3.1 was achieved at 1 A. However, operation in hot environments necessitates increased current to maintain low absorption temperatures, leading to a critical "thermal runaway" threshold beyond 5 A where internal Joule heating (scaling quadratically) outweighs the Peltier cooling effect (scaling linearly). While both platforms effectively evaluate heat transfer, the Python-based empirical model provided a more realistic description of cold-side absorption with prediction errors as low as 0.14%. These findings offer a robust pathway for optimizing Peltier cooling with potential industrial applications.

**Keywords:** Peltier; Python; MATLAB Simulink; thermoelectric effect; thermoelectric efficiency

## 1. Introduction

Global energy demand continues to rise unabated, but over-reliance on non-renewable energy sources has triggered severe ecological crises, including global warming and systemic climate change [1,2]. Consequently, the growing demand for precise thermal management has placed Peltier modules at the forefront of solid-state cooling solutions [3,4]. A typical module consists of multiple p-type and n-type semiconductor pairs acting as thermocouples [3,5,6]. These elements are thermally connected in series to minimize thermal resistance and electrically connected in series to increase the operating voltage, all sandwiched between two insulating ceramic plates [7–9]. Operating as a solid-state heat pump through the Peltier effect, the device creates a temperature gradient by absorbing heat at one face and dissipating it at the other when an electric current passes through the p-n junctions [10–13]. Although its low coefficient of performance originally restricted applications to specialized scientific, aerospace, and medical equipment [14], this technology is increasingly deployed in consumer comfort systems, such as portable refrigerators, electronic circuit coolers, and automotive seat climate controls [15]. Conversely, in power

Check for updates

Academic Editor: Christos Douligeris

Received: 22 May 2026
Revised: 17 July 2026
Accepted: 30 July 2026
Published: 10 August 2026

**Copyright:** © 2026 by the authors. Published by MDPI on behalf of the International Institute of Knowledge Innovation and Invention. Licensee MDPI, Basel, Switzerland. This article is an open access article distributed under the terms and conditions of the Creative Commons Attribution (CC BY) license.

generation mode via the Seebeck effect, maintaining a temperature difference across the module induces an electromotive force to generate electricity [16,17].

The value of these converters lies in their lack of moving parts, low noise, compactness and high reliability [18–20]. Maximizing the potential of these converters requires robust modeling that transcends simple heat transfer equations to accurately analyze energy efficiency across both operating modes [21,22]. These simulation techniques facilitate the analysis, design, and optimization of single or multi-module thermoelectric systems for specific applications [23,24]. Currently, equivalent circuit models are frequently developed using SPICE software to establish a direct equivalence between thermal and electrical networks for high-fidelity simulations [25–29]. Similarly, MATLAB/Simulink is widely utilized to construct a block-based models [4,30,31]. This interface-driven approach allows engineers to accurately predict voltage and current requirements for a given temperature gradient (ΔT) using minimal input parameters, bypassing the need for exhaustive experimental datasets [32–35]. Beyond single-mode operation, dual purpose systems have also been developed to utilize Peltier modules as both heat pumps and thermoelectric generators [36–38].

This study implements mathematical modeling of the electrical and thermal behavior of Peltier modules using two distinct platforms: Python3.11 and MATLAB/Simulink R2018b. Both approaches utilize experimental datasets encompassing heat sink performance, heat absorption, heat dissipation, and the COP. A critical operational focus of this work is the isolated impact of ambient temperature on module efficiency.

The proposed modeling approach establishes a new comparative network based on three items: (a) systematically isolating the performance of commercial off-the-shelf (COTS) Peltier modules under realistic tropical ambient constraints (28–40 °C); (b) while traditional numerical solvers and SPICE-equivalent circuits rely on multi-layered differential iteration loops with high computing overhead, the proposed Python-based model achieves a highly streamlined $O(1)$ execution complexity; and (c) through precise regression mapping of our experimental data, we identified a distinct physical symmetry in the dual-quadratic temperature evolution coefficients of the hot and cold junctions. Consequently, this dual-platform investigation bridges the gap between top-down theoretical design sizing (via MATLAB/Simulink) and bottom-up empirical operational control (via Python), offering a comprehensive optimization tool for modern solid-state thermal management systems operating in harsh environments. Furthermore, this paper demonstrates the capacity of a lightweight, open-source Python framework to accurately replicate dynamic physical behavior, establishing a robust pathway for evaluating sophisticated control strategies and optimizing the efficiency of modern thermal systems.

## 2. Materials and Methods

### *2.1. Voltage–Temperature Coupling and Dual-Quadratic Regression Methodology*

To characterize the thermal behavior of the commercial thermoelectric module, an experimental data-driven modeling methodology was developed based on voltage–temperature (V-T) coupling analysis and dual-quadratic regression mapping. Unlike conventional approaches that require detailed temperature-dependent material properties or proprietary manufacturing parameters, the proposed framework utilizes directly measurable operating variables, namely applied voltage and junction temperatures, to establish a physically representative model of device performance. Experimental measurements were acquired under controlled operating conditions covering the complete voltage range of the module. The resulting dataset was used to determine the thermal evolution of both hot-side and cold-side junctions through second order polynomial regressions. Model coefficients were identified using least-squares optimization, and the resulting parameter sets were

subsequently incorporated into energy-balance formulation of the thermoelectric system. A key feature of the methodology is the introduction of a V-T coupling coefficient that captures the influence of electrical excitation on thermal behavior while accounting for practical packaging effects and boundary conditions inherent to commercial-off-the-shell (COTS) devices. The predictive capability of the proposed model was evaluated through statistical validation procedures.

### *2.2. Operational Principles and Governing Equations of Thermoelectric Modules*

The operation of a thermoelectric module involves four primary physical processes: the Fourier effect (thermal conduction), the Joule effect, the Peltier effect (cooling), and the Thompson effect [34,39–41]. Thermal conduction occurs due to the temperature gradient between the hot side ($T_h$) and cold side ($T_c$) and is defined by the thermal resistance between both sides of the Peltier module ($R_p$) [42].

$$Q_{Fr} = \frac{T_h - T_c}{R_{th}} = \frac{\Delta T}{R_{th}} \quad (1)$$

The temperature gradient generated on both sides of the Peltier module is caused by the electrical current applied to the Peltier cells or semiconductor thermocouples. The higher the thermal resistance of the Peltier module, the lower the heat flow for the same temperature gradient [43].

When current (I) flows through the module, the Joule effect causes energy dissipation in the form of heat, distributed equally between both faces [44]:

$$Q_J = \frac{R_e}{2} \cdot I^2 \quad (2)$$

where $R_e$ ($\Omega$) is the equivalent electrical resistance of the Peltier module, and I represent the electrical current that passes through the module. The Peltier cooling–heating effect is a phenomenon of heat absorption–dissipation produced by the union of two different materials when electric current flows through this union [45]. Heat absorbed $Q_{Pc}$ and dissipated $Q_{Ph}$ by union (Watts) is defined as follows:

$$Q_{Pc} = S \cdot I \cdot T_c \quad (3)$$

$$Q_{Ph} = S \cdot I \cdot T_h \quad (4)$$

where S in the equation is defined as the Seebeck coefficient of the Peltier module (V $K^{-1}$). The net heat flux absorbed by the cold side and dissipated by the hot side, accounting for conduction and Joule heating, can also be expressed as [46–48]:

$$Q_{net,c} = Q_{Pc} - Q_J - Q_{Fr} \quad (5)$$

$$Q_{net,c} = SIT_c - \frac{R_e}{2} I^2 - \frac{T_h - T_c}{R_{th}} \quad (6)$$

$$Q_{net,h} = SIT_h - \frac{R_e}{2} I^2 - \frac{T_h - T_c}{R_{th}} \quad (7)$$

The total electrical power ($P_e$) consumed is the difference between these fluxes, and the required input voltage (V) is determined by the Seebeck voltage and the internal resistance [49]:

$$P_e = Q_{net,\,h} - Q_{net.\,c} = SI(T_h - T_c) + I^2 R_e \quad (8)$$

$$V = S(T_h - T_c) + IR_e \quad (9)$$

The efficiency of the system is measured by the COP, defined as the ratio of cooling provided to the power consumed [49]:

$$COP = \frac{Q_{net,c}}{P_e} \tag{10}$$

In cooling operations, a heat sink with the lowest possible thermal resistance must be attached to the hot side, (Figure 1a,b). Without effective dissipation, $T_h$ rises, which significantly reduces the $Q_{net,c}$ and the COP. Finally, these modules are modeled as thermal systems using thermal resistance ($R_{th}$) and thermal capacity (C), where capacity defines the heat required to change the body's temperature (dT) over time (dt) [50,51]:

$$C = \frac{dQ}{dT} \Rightarrow \frac{dT}{dt} = \frac{Q_{in}}{C} \tag{11}$$

$$C \cdot \frac{dT}{dt} = Q(t) \Rightarrow T(t) = T(0) + \frac{1}{C} \cdot \int_0^t Q(t) \tag{12}$$

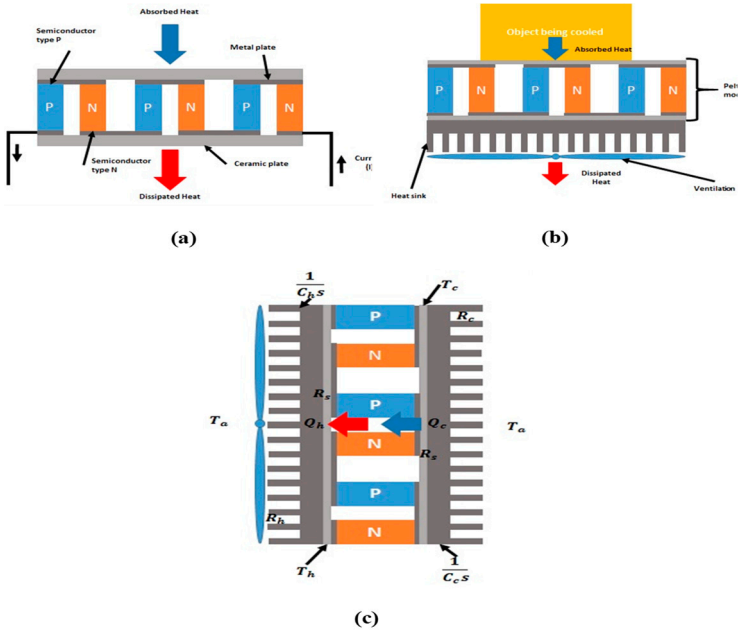



**Figure 1.** Schematic representation of Peltier module, (**a**) components, (**b**) heat transfer along the module, (**c**) thermal capacitances analyzing the absorption and dissipation of heat in Peltier cooling system.

Thus, the novelty of this study lies in the mathematical mapping real-world packaging and thermal boundary conditions via a generalized voltage–temperature (V-ΔT) coupling coefficient combined with a dual-quadratic parameter tracking approach. This approach bypasses the limitations of commercial off-the-shelf (COTS) modules.

### *2.3. Model Building*

The model incorporates heat sinks on both the cold (absorption) and hot (dissipation) sides of the Peltier module [52]. Heat dissipation on the hot side is achieved through forced convection via integrated fans. Furthermore, the interface between the heat sinks and the module includes the thermal resistance of the applied thermal paste. By accounting for these physical components, the model generates key thermal parameters: the thermal resistances ($R_c$ and $R_h$) and thermal capacities ($C_c$ and $C_h$) for both sides, along with the contact resistance ($R_s$) of the thermal interface material. The network of thermal resistances and capacities governing heat exchange between the module faces and the ambient environment is presented in Figure 1c.

Assuming each heat sink is isothermal, their respective thermal masses can be modeled as capacitive elements. By applying the energy balance represented in Equation (11) to both the cold and hot sides of the module and performing a Laplace transform, the sys-

tem's dynamic behavior is characterized [53]. This yields the following transfer functions, which define the relationship between the heat flux and the temperature response in the frequency domain:

$$\frac{T_h - T_a}{Q_h} = \frac{R_h + R_s}{1 + C_h \cdot s \cdot (R_h + R_s)} \tag{13}$$

$$\frac{T_a - T_c}{Q_c} = \frac{R_c + R_s}{1 + C_c \cdot s \cdot (R_c + R_s)} \tag{14}$$

where $T_a$ (K) is the room temperature, and $R_h$ (K/W) and $R_c$ (K/W) denote the thermal resistance of the hot and cold sides of the Peltier module relative to the surrounding air, respectively. $C_h$ and $C_c$ are the thermal capacities of the heat sinks on the hot and cold sides, and $s$ is the Laplace operator used to transform the differential equations into the complex frequency domain (transfer functions).

It should be noted that the thermal capacity is a function of the heat sink's physical dimensions and material properties, whereas the thermal resistance is governed by the following factors [54]: (i) the thermal contact resistance between the Peltier module and the heat sink (dependent on the interface material), (ii) the specific geometry and design of the heat sink model, and (iii) the fan supply voltage, which dictates the airflow velocity and, consequently, the convective heat transfer coefficient.

Once the governing principles and mathematical expressions of the Peltier module were established, a block-based model was developed to simulate these dynamics within both Python and MATLAB/Simulink environments [55–57]. The process of heat transfer through the Peltier module used in this study was summarized in Figure 2. This diagram involves a complex interaction between active thermoelectric transport and passive thermal losses. The model accounts for the Seebeck effect, which drives the cooling, while simultaneously subtracting the penalties imposed by internal Joule heating and parasitic thermal conduction.

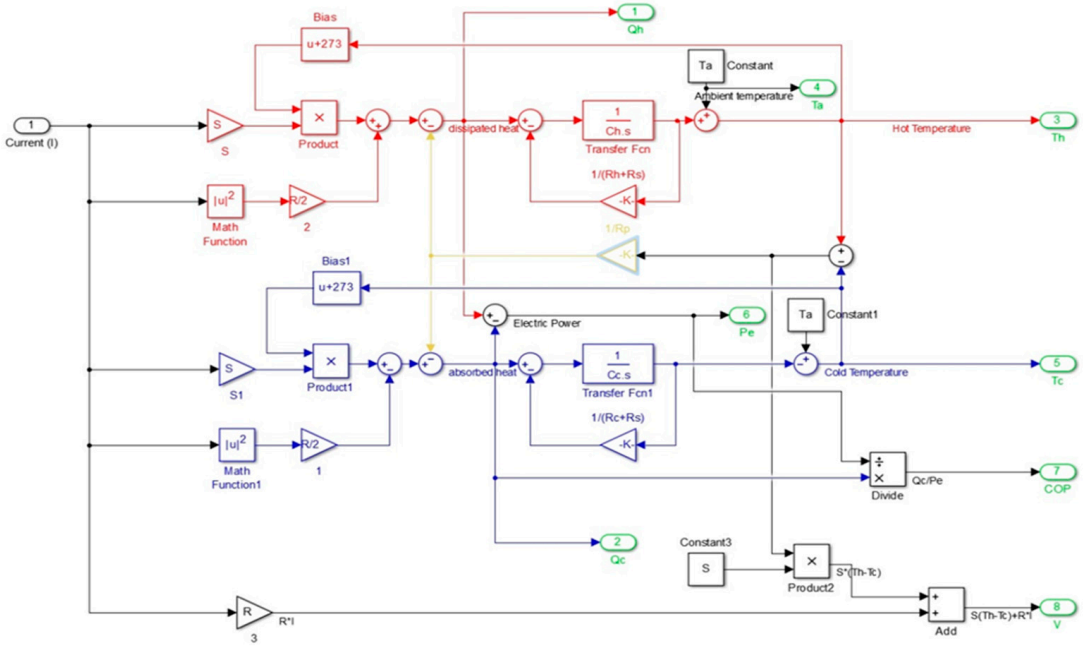



**Figure 2.** Peltier module connections for heat transfer evaluation.

### *2.4. Calculation of the Thermoelectric Module Parameters*

Commercial manufacturers characterize Peltier modules using a set of specific operational limits [58–61]. ΔT: The maximum temperature difference is achievable between the hot and cold junctions when the cooling capacity is zero ($Q_c = 0$). $Q_{c,\,max}$: The maximum

heat absorption capacity of the module, occurring when the temperature difference between the faces is zero ($\Delta T = 0$). $I_{max}$: The maximum input current the module can sustain without reaching thermal saturation or damaging the internal semiconductor junctions. $V_{max}$: The maximum voltage applied to the Peltier module. Then, in consequence, the electrical and thermal characteristics of the Peltier module used to perform the simulation in this study were defined in Table 1.

**Table 1.** Electrical and thermal characteristics of the Peltier module.

| Hot-Side Temperature $T_h$ (°C) | 27 °C | 50 °C |
|---|---|---|
| $Q_{c,\,max}$ (Watts) | 61.4 | 66.7 |
| $\Delta T_{max}$ (°C) | 70 | 79 |
| $I_{max}$ (Amps) | 6 | 6 |
| $V_{max}$ (Volts) | 16 | 17.2 |
| Rth (Ohms) | 1.8–2.2 | 2.0–2.4 |

To bridge the gap between the manufacturer's data sheet specifications and the internal parameters required for the simulation, Equations (15)–(18) were employed [41,49,62]. These expressions derive the Seebeck coefficient (S), the internal electrical resistance ($R_e$), the thermal resistance (Rth) and thermal conductance ($K_m$) of the Peltier module. By integrating these calculated material properties, the model accurately replicates the coupled thermoelectric behavior of the device [63].

$$S = \frac{V_{max}}{T_h} \tag{15}$$

$$R_e = \frac{(T_h - \Delta T_{max})V_{max}}{T_h I_{max}} = \frac{V_{max} - S\Delta T_{max}}{I_{max}} \tag{16}$$

$$R_{th} = \frac{\Delta T_{max}}{I_{max} V_{max}} \frac{2T_h}{(T_h - \Delta T_{max})} \tag{17}$$

$$K_m = \frac{1}{R_p} = \frac{(T_h - \Delta T_{max}) - V_{max}\ I_{max}}{2T_h \Delta T_{max}}. \tag{18}$$

Applying Equations (15)–(17) to the manufacturer data provided in Table 1 (at a reference hot-side temperature $T_h$ = 50 °C), the following characteristic parameters for the thermoelectric module were derived for use in the simulations: Seebeck Coefficient (S) = 0.0532 V $K^{-1}$, Electrical Resistance ($R_e$) = 2.13 Ω and Thermal Resistance (Rth) = 1.99 K $W^{-1}$.

Furthermore, the thermal capacitances of the cold-side ($C_c$) and hot-side ($C_h$) heat sinks are fundamental to the transient of system response. These values are determined using the following relation:

$$C = c\rho v \tag{19}$$

where C is the thermal capacity (J $K^{-1}$), c is the specific heat of the material (kJ $kg^{-1}$ $K^{-1}$), $\rho$ is the density (kg $m^{-3}$), and $v$ the volume in $m^3$ of the heat sink. Therefore, these heat sinks are represented by the values $C_c$ and $C_h$.

The parameters governing a Peltier module's performance can be categorized into three distinct groups [64–66]. First are the intrinsic constants (such as maximum cooling capacity ($Q_{c,\,max}$), temperature differential ($\Delta T_{max}$), and peak electrical ratings ($I_{max}$, $V_{max}$), which are determined by the material quality and manufacturing process. These are typically provided in technical data sheets of the manufacturer. Second are the derived parameters, including internal electrical resistance, thermal resistance, and the Seebeck coefficient, which are calculated from the data sheet constants. Finally, the extrinsic parameters are defined by the physical cooling assembly. The thermal capacities ($C_h$, $C_c$) depend

on the specific heat sinks utilized, while the thermal resistances relative to the environment are dictated by the airflow characteristics of the integrated fans. Additionally, the thermal interface resistance accounts for the properties of the thermal grease applied between the module faces and the heat sinks. With this information, the specific values used to develop and simulate the model in Simulink are presented in Table 2. It is important to highlight that this modeling framework is designed to allow for the dynamic variation in supply current and ambient temperature.

**Table 2.** Values used in the simulation.

| Parameters | Value |
|---|---|
| Seebeck Coefficient (S) | 0.0532 V $K^{-1}$ |
| Electric Resistance ($R_e$) | 2.13 Ω |
| Peltier module thermal resistance (Rth) | 1.99 K $W^{-1}$ |
| Hot-side thermal capacity ($C_h$) | 378.4 J $K^{-1}$ |
| Cold-side thermal capacity ($C_c$) | 378.4 J $K^{-1}$ |
| Hot-side thermal resistance ($R_h$) | 0.15 K $W^{-1}$ |
| Cold-side thermal resistance ($R_c$) | 1 K $W^{-1}$ |
| Silicone grease thermal resistance ($R_s$) | 1.14 K $W^{-1}$ |

### *2.5. Model Validation*

To validate the proposed model, the simulated behavior was compared against the manufacturer's performance curves using the same reference parameters. In Figure 3, the simulated temperature differential ($\Delta T$) and supply voltage (left) appear slightly lower than the values provided in the technical data sheet (right) for identical current inputs.

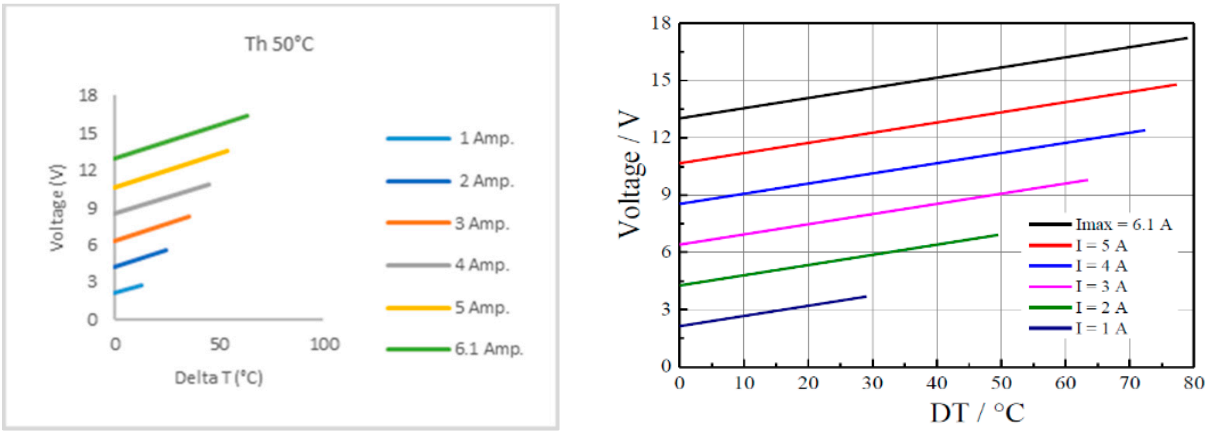



**Figure 3.** Behavior of the voltage supplied to the Peltier module, related to difference in temperature between the hot and cold side, and the electric current.

This discrepancy is primarily due to the inclusion of real-world thermal resistances ($R_h$, $R_c$, and $R_s$) and thermal capacities in the simulation model [67]. As noted by X. Hao et al., a higher thermal resistance on the hot side restricts heat dissipation, which subsequently reduces the achievable $\Delta T$ between the junctions [68]. Because the simulation accounts for these experimental thermal losses, the resulting voltage required, as governed by Equation (11), is also lower. Even with these differences, the simulation data is very close to that presented in the graph of the technical data sheet of the module that was used as a reference. The model indicated that reaching a maximum differential of 61.1 °C requires a power input of 16.2 V and 6 A.

Similarly, Figure 4 compares the heat absorption capacity ($Q_c$) as a function of ΔT and input current. Both the simulation (left) and the data sheet (right) show that the maximum

heat absorption occurs when $\Delta T = 0$ for a given current. The slight variations observed between the two graphs stem from the influence of the cold-side thermal capacity and the hot-side thermal resistance [68]. Consistent with thermoelectric theory, while increasing the current enhances heat absorption, a rising temperature gradient across the module creates a parasitic backflow of heat, thereby reducing the net $Q_c$ under constant current conditions.

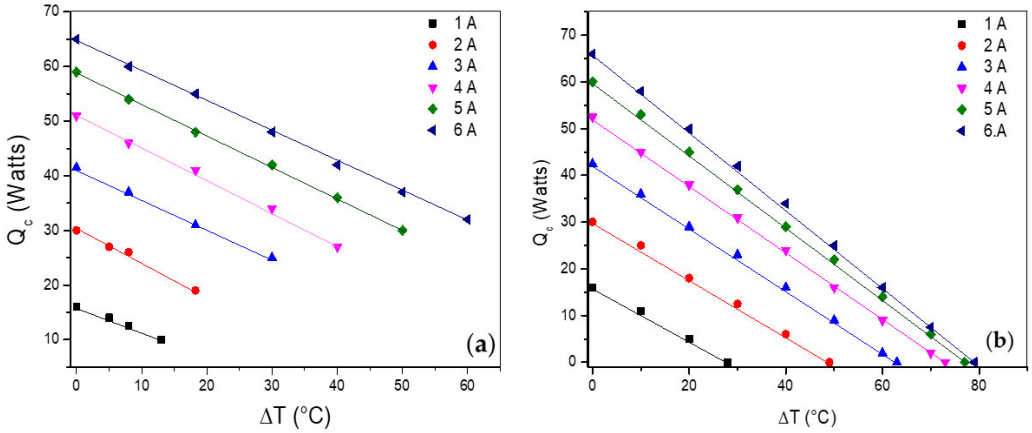



**Figure 4.** (**a**) Heat absorbed with respect to temperature difference between the hot and (**b**) cold-side of the Peltier module and the current supplied.

To establish a robust, data-driven alternative to proprietary manufacturer constants, the Python-based framework utilizes a linear least-squares regression matrix to solve the non-linear coupling coefficients governing the module's boundary conditions. The dynamic temperature profiles of the hot face ($T_h$) and cold face ($T_c$) are modeled using a dual-quadratic parameter tracking approach. The model parameters were derived strictly using a training dataset (70% of collected profiles). Crucially, the remarkably low error metrics reported in the manuscript were obtained by testing the model against an entirely independent verification dataset (30% of data withheld during fitting) across all current steps (1–6 A) and ambient sweeps (28, 32, 36, and 40 °C).

### *2.6. Computational Implementation in Python*

The experimental phase was conducted using a commercial Peltier module with specifications matching those presented in Table 1. The experimental setup included: (a) a controlled ambient temperature environment (40 °C initial temperature), (b) high-precision temperature sensors on both hot and cold sides, (c) calibrated voltage and current measurements, and (d) a data acquisition system for continuous monitoring. Data collection was performed at four distinct current levels: 1. Low current (1 A)—representing minimal cooling operation, 2. Medium current (3 A)—typical operating condition, 3. Medium-high current (4.5 A)—enhanced cooling operation, and 4. High current (6 A)—maximum rated operation. For each current level, measurements were recorded for hot-side temperature ($T_h$), cold-side temperature ($T_c$), temperature difference ($\Delta T$), and applied voltage (V).

The sampling interval was optimized to capture both rapid initial changes and steady-state behavior, with measurements taken until thermal equilibrium was achieved at each current level. A consistent linear relationship between voltage and temperature difference emerged across all current levels, following a general straight equation considering practical features (Supplementary Materials).

It is important to clarify that the core thermal balance framework of the thermoelectric system does not rely on Partial Differential Equations (PDEs) that necessitate numerical grid solvers. Instead, the transient behavior of the Peltier module and its attached heat sinks is governed by a Lumped Element Thermal Capacitance (C) and Resistance (R) net-

work, which yields a coupled system of linear Ordinary Differential Equations (ODEs). To ensure mathematical rigor without relying on iterative numerical approximations for the baseline, an exact analytical solution was derived. By applying the Laplace transform to these time-dependent governing ODEs, the system was mapped into the complex frequency domain (s-domain). This yielded the closed-form, analytical transfer functions detailed in Equations (13) and (14), which directly define the dynamic junction temperatures ($T_h$ and $T_c$) relative to the thermal flux inputs ($Q_h$ and $Q_c$). These analytical equations form the mathematical foundation for the block inputs within the Simulink environment.

### *2.7. Model Validation and Comparison with Simulink*

Experimental Validation

Detailed validation was performed at each current level. For example, the 4.5 A case, displayed the values of Table 3.

**Table 3.** Values obtained at 4.5 A.

| Parameter | Experimental | Model Prediction | Error (%) |
|---|---|---|---|
| ΔT (max) | 2.210 °C | 2.207 °C | 0.14 |
| V (init) | 8.865 V | 8.865 V | 0.00 |
| V (final) | 8.977 V | 8.978 V | 0.01 |
| $T_h$ (max) | 41.405 °C | 41.410 °C | 0.01 |
| $T_c$ (min) | 39.198 °C | 39.200 °C | 0.01 |

It is important to highlight that the Simulink models are based on the following considerations: this environment was used as an interface-driven, solver-based platform to construct a macro-level block model based on standard thermoelectric governing equations. It acts as a robust baseline for ideal thermodynamic parameter optimization, steady-state sensitivity analysis, and prediction of macro-scale electrical requirements using manufacture data sheets. However, it operates under the assumption of ideal material properties and carries a high computational overhead and licensing dependency, which makes it less suitable for direct hardware embedding.

Python: Experimental data and empirical relationships require only current input and desired temperature range. Accuracy Characteristics: Better for practical performance prediction in real operating conditions. Computational requirements: Lightweight, open-source implementation. Adaptation to Different Modules: can be adapted through simple coefficient adjustments Advantages: direct incorporation of real-world behavior, accounts for non-ideal effects automatically and high accuracy within the tested range. Implementation Benefits: simple parameter inputs, fast computation time, easy integration with other systems and Excel output for practical use. Flexibility: easy modification for different modules, simple adaptation to new operating conditions and scalability to different temperature ranges. Limitations: limited to tested current range (1–6 A), validated for specific temperature range and requires recalibration for different ambient conditions. Model Assumptions: Linear voltage–temperature relationship, quadratic temperature evolution, constant ambient temperature. The Python-based framework functions as a lightweight, open-source, data-driven tool, by deploying an empirical voltage–temperature (V-ΔT) coupling coefficient from experimental datasets. It bypasses the limitations of proprietary, temperature-dependent, internal material parameters (e.g., precise internal thermal conductivity or electrical resistivity) that are often omitted in commercial specifications.

In this context, the study proposed Simulink to obtain the necessary foundation for validation against idealized thermoelectric theory, whereas the Python model is optimized for real-active thermal management. Its lightweight $O(1)$ computational efficiency makes it mathematically suitable for direct integration into physical microcontrollers to execute

rapid pulse-width modulation control loops in practical applications, as it is the case in this work.

## 3. Results

### *3.1. System Configuration and Modeling Parameters*

Numerical simulations were conducted to characterize the steady-state and transient performance of a standard commercial Peltier module. The physical domain integrated aluminum heat sinks on both the hot and cold junctions, with an active cooling fan on the hot-side assembly to optimize heat rejection. To address the specific operational constraints of these devices, the chosen temperature domain (38 °C to 50 °C hot-side evolution under 28 °C to 40 °C ambient) was selected to systematically isolate the effects of tropical climates and high-temperature industrial environments on solid-state cooling efficiency. While individual temperature sweeps are common in thermoelectric characterizations, evaluating the coupled interactions between high ambient thermal loads ($T_{amb}$ = 40 °C) and severe electrical input current variations provides a valuable baseline that standard ambient evaluations lack. Therefore, the study evaluated performance across two critical independent variables: (i) Ambient temperature: varied from 28 °C to 40 °C to simulate operation in tropical climates and high-temperature industrial environments. (ii) Supply Current: Modeled as a step function from 1 A to 6 A, facilitating the analysis of both transient thermal evolution and steady-state equilibrium.

Finally, to ensure high-fidelity thermal modeling, the thermal contact resistance ($Rth_{,c}$) of the thermal interface material (TIM) was accounted for at all module-heat sink interfaces, bridging the gap between idealized theory and real-world implementation.

### *3.2. Thermal Flux Analysis ($Q_c$ and $Q_h$)*

The thermal behavior, specifically heat absorption at the cold junction ($Q_c$) and heat dissipation at the hot junction ($Q_h$), is illustrated in Figure 5. Results indicate that both $Q_c$ and $Q_h$ correlate positively with ambient temperature. However, as supply current increases, $Q_h$ increases at a significantly higher rate than $Q_c$. This divergence is fundamentally driven by Joule heating ($I^2R$). While the Peltier effect (cooling) scales linearly with current, Joule heating scales quadratically. Consequently, the hot side must reject the sum of the pumped heat and the internal resistive losses.

By investigating how the module behaves as hot-side temperatures approach 50 °C, we uncovered a critical performance phenomenon that only occurs during high ambient operations. As the performance curves demonstrate, running the system in a 40 °C ambient environment shifts the net cooling capacity ($Q_c$) significantly downward compared to standard room-temperature setups. Testing within this specific operational window is exactly what allows us to mathematically describe the thermal runaway boundary that occurs right beyond 5 A. At this specific threshold, the quadratic growth of internal joule heating ($I^2R_e$) completely overwhelms the linear thermoelectric cooling effect (S I $T_c$). Beyond 5 A under these specific temperature limits, the system shifts into a heat-dominant regime: cooling capacity completely collapses, and the hot-side thermal load surges to an extreme 122 W. Isolating this transition point is vital, as it provides concrete guidance for engineers developing applications tailored to hot geographic regions.

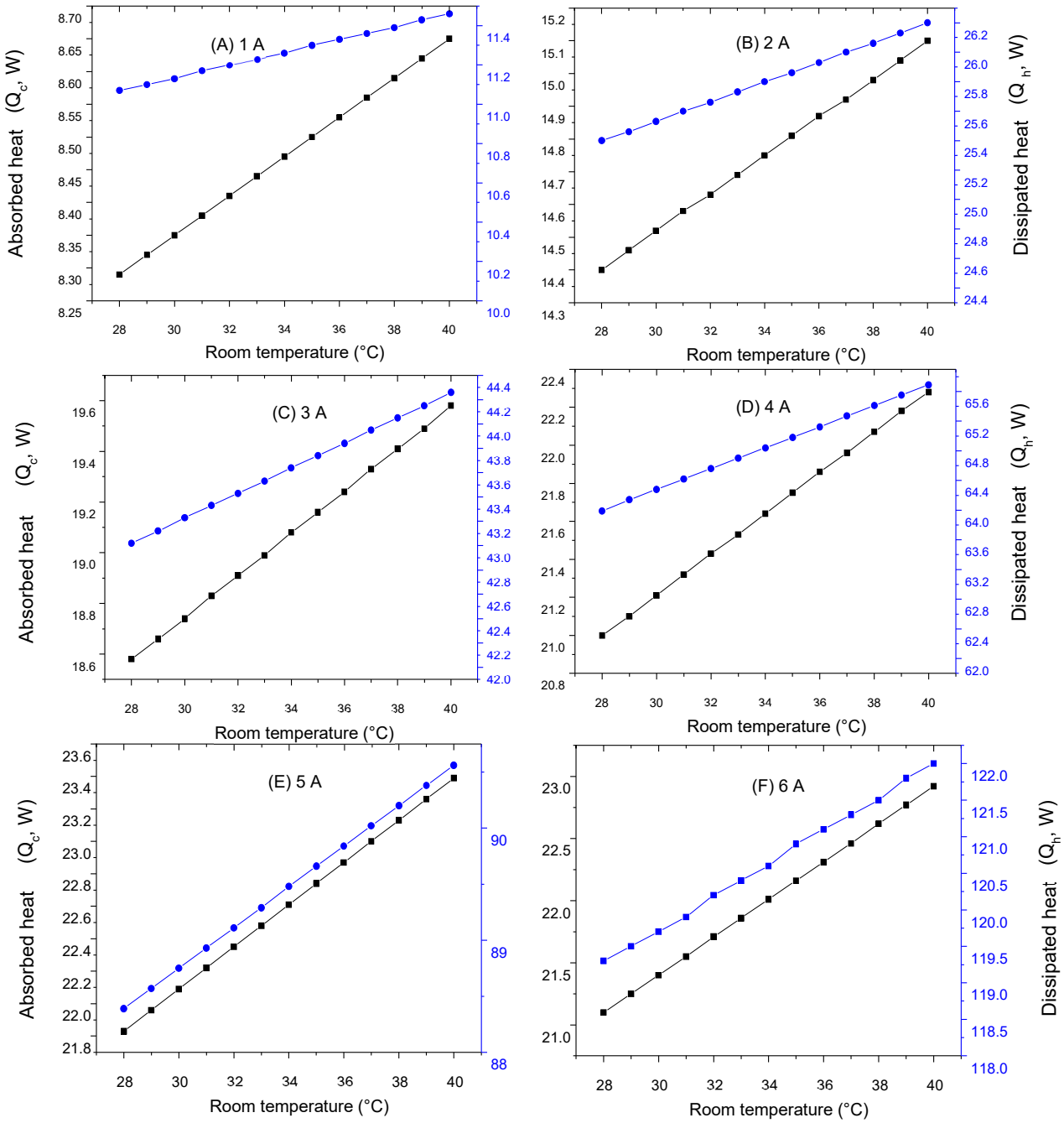



**Figure 5.** Heat absorbed and dissipated by the Peltier module under temperature variation (28 °C (blue lines) and 40 °C black lines) and increasing electric current from 1 to 6 A (upper left to lower right).

### *3.3. Junction Temperature and ΔT Evolution*

Figure 6 displays the temperature of the cold ($T_c$) and hot ($T_h$) junctions of the Peltier module as a function of ambient temperature and supply current. As current increases, the temperature differential (ΔT) expands; $T_c$ decreases while $T_h$ rises sharply. The minimum cold junction temperature achieved was 3.7 °C at $T_{amb}$ = 28 °C and I = 5 A. At a constant current, rising ambient temperatures result in a proportional rise in both junction temperatures. Thus, lowering $T_c$ in high-ambient environments requires significantly higher electrical power to overcome the external thermal load, often at the cost of efficiency.

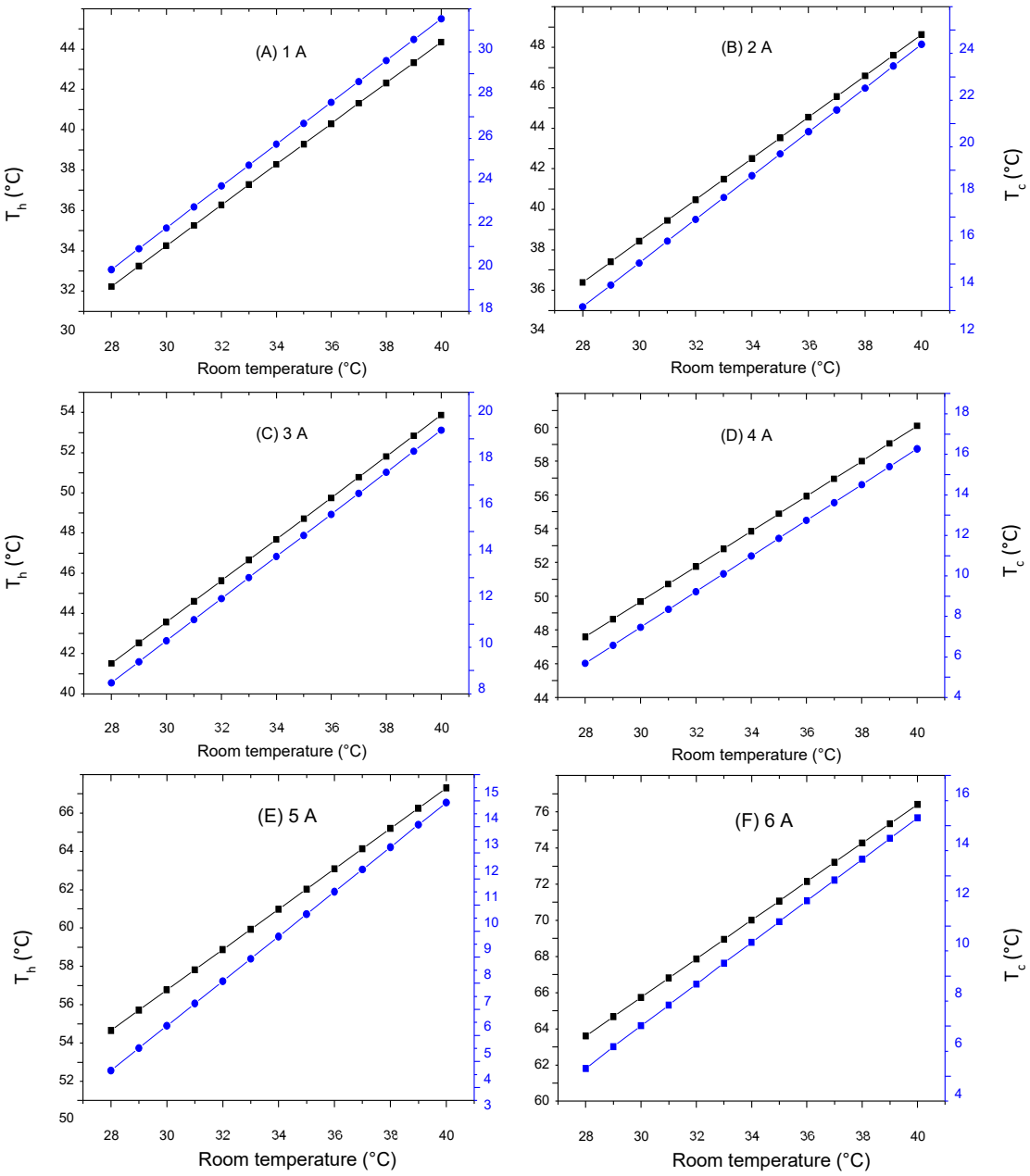



**Figure 6.** Cold-side and hot-side temperature of the Peltier module obtained when operated at a variable room temperature (28 °C to 40 °C) and with an increase in electric current from 1 to 6 A (upper left to lower right).

As illustrated in Figure 7, a critical operational divergence occurs beyond 5 A at an ambient temperature of 40 °C. While cooling capacity ($Q_c$) scales moderately by 16% per ampere up to 5 A (23.4 W), the hot-side heat load ($Q_h$) escalates sharply by an average of 37% per ampere due to the quadratic nature of the Joule heating ($I^2R_e$): increasing the input current to 6 A forces the system past its optimal thermodynamic threshold into a heat-dominant regime. At this stage, internal thermal backflow completely overwhelms the linear Peltier effect, causing a 2% drop in net heat absorption (22.9 W) alongside a 25.7% surge waste heat dissipation, which reaches an extreme value of 122 W.

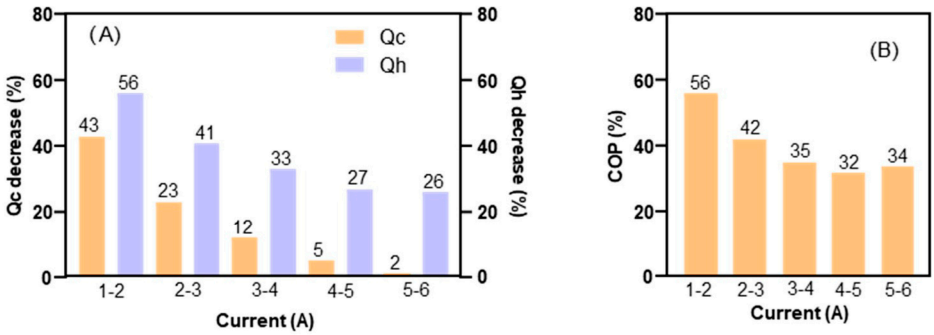



**Figure 7.** (**A**) Variation (%) of heat absorbed and heat dissipated; (**B**) coefficient of performance with respect to the increase in electric current at temperature of 40 °C.

In Table 4, the ratio of heat dissipation to heat absorption was analyzed. For each unit of electric current, the dissipated heat increases by an average of 57% relative to the absorbed heat. Starting at a current of 3 A, a significant surge in heat dissipation is observed, eventually reaching levels five times higher than the absorbed heat at a current of 6 A.

**Table 4.** Increase in heat dissipated with respect to heat absorbed at ambient temperature of 40 °C (%).

| **% Increase $Q_c$ over $Q_f$** | |
|---|---|
| Electric current | % increase Qh-Qc |
| 1 | 24.5 |
| 2 | 42.4 |
| 3 | 55.8 |
| 4 | 66.1 |
| 5 | 74.2 |
| 6 | 81.2 |
| Average | 57 |

Figure 8 plots the junction temperature profiles ($T_h$ and $T_c$) as a function of current and environmental shifts: due to high external ambience loads, progressively higher operating currents are required to force down the cold junction temperature ($T_c$). A maximum temperature gradient ($\Delta T$) of 61.1 °C was achieved at a peak current of 6 A, highlighting that sub-ambient cooling capacity remains heavily contingent upon the forced convection efficiency of the hot-side heat sink assembly.

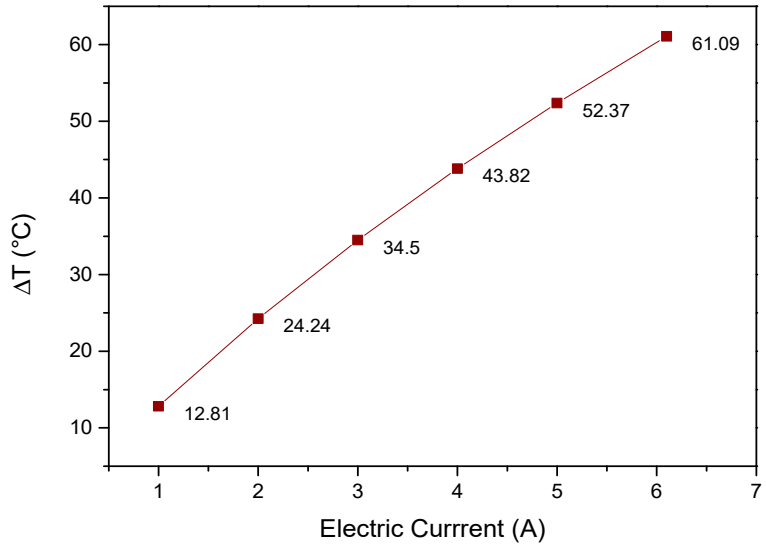



**Figure 8.** Temperature difference between the hot and cold side of the thermoelectric module used.

Figure 9 illustrates the behavior of the coefficient of performance (COP), as well as the heat absorbed and dissipated by the module, as a function of both ambient temperature and supply current. A higher COP signifies a more efficient utilization of electrical energy for heat absorption; essentially, a larger portion of the supplied electricity is used for cooling rather than being lost as dissipated heat.

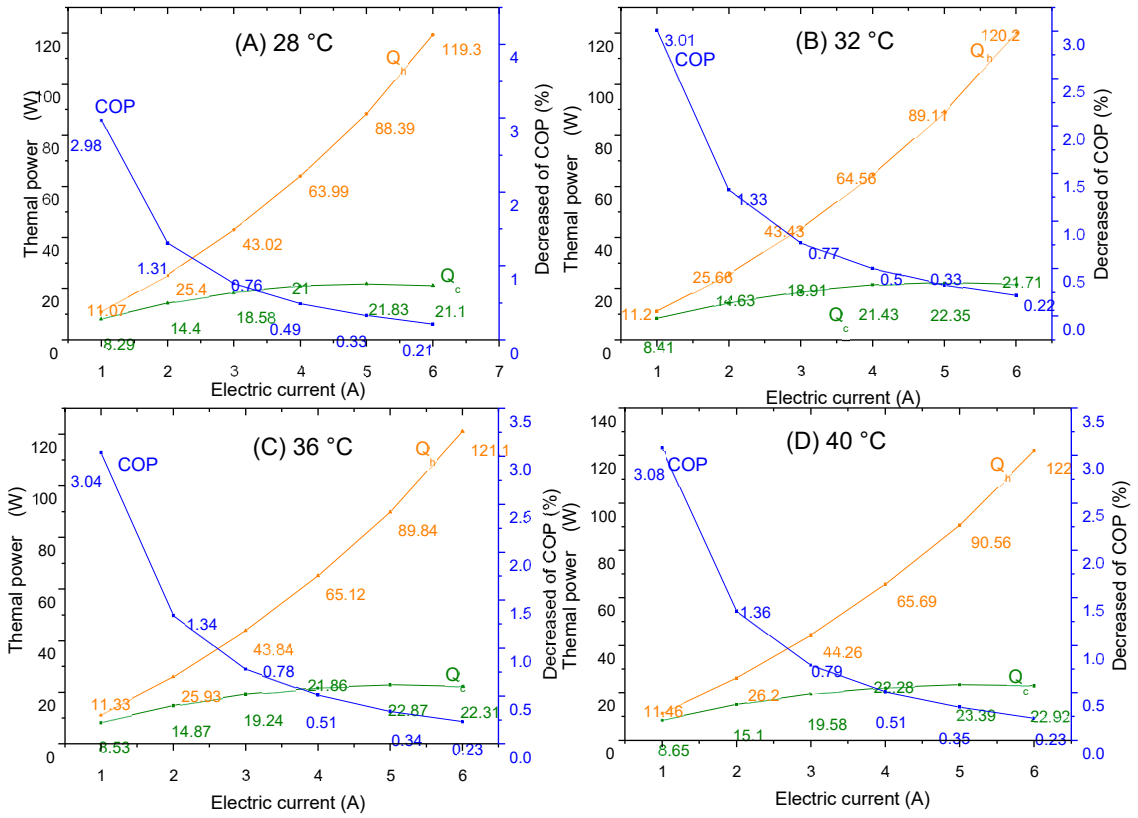



**Figure 9.** Heat absorbed ($Q_c$) and heat dissipated ($Q_h$) in the Peltier module and COP efficiency against electric current supplied at (**A**) 28 °C, (**B**) 32 °C, (**C**) 36 °C and (**D**) 40 °C.

The maximum COP of 3.1 was observed at a supply current of 1 A and an ambient temperature of 40 °C. Under these conditions, for every watt (W) of electrical power supplied, the cold side absorbed 3.1 times that amount in thermal energy. Conversely, the minimum COP recorded was 0.21, occurring at a supply current of 6 A and an ambient temperature of 28 °C. These results demonstrate that the module operates with significantly higher efficiency at lower current supplies.

The COP is also heavily dependent on the efficiency of the heat sink coupled to the hot side of the Peltier module. Standard air-cooled heat sinks (forced convection) typically provide thermal resistances ranging from 0.5 to 0.7 [69,70], whereas water-cooled systems can achieve values as low as 0.1 K $W^{-1}$ [71]. A lower thermal resistance at the hot side facilitates greater heat absorption [72] and a higher COP, as it allows the Peltier module to maximize the conversion of electrical energy into effective thermal transport.

It can be seen in Figure 10 how the COP varies with respect to the supply current and the temperature difference; the higher the supply current, the lower the COP, since the electric power supplied increases and, therefore, more heat is dissipated at the hot side of the module; meanwhile, heat absorption increases moderately. This can also be observed in Figure 9. Correspondingly, as the temperature difference between the cold and hot sides of the module increases, the COP coefficient decreases; thus, the module will operate with higher performance when the temperature difference between both sides

is smaller. As previously mentioned, during the simulations, the maximum COP was 3.1 with a current of 1 A of power supplied to the module, while the lowest performance was 0.21 with 6 A.

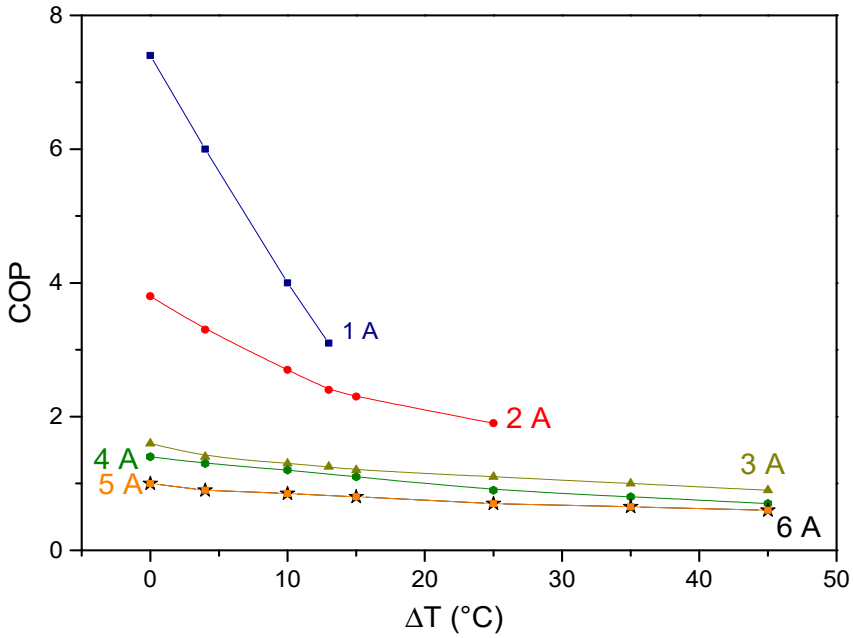



**Figure 10.** COP compared to the difference in temperature and electric current.

The core finding of this study is the identification of the critical current (I~5 A) at an ambient temperature of 40 °C. In thermoelectric theory, the cooling power ($Q_c$) is a parabolic function of current according to the following equation:

$$Q_c = SIT_c - \frac{1}{2}I^2R_e - K\Delta T \quad (20)$$

where $S$ is the Seebeck coefficient, $R_e$ is electrical resistance, and $K$ is thermal conductance.

Based on this information, the results demonstrate that at 6 A, the internal $I^2R_e$ term increases by 25.7% while the first term ($SIT_c$) fails to compensate, leading to a net reduction in $Q_c$. This confirms that operating a Peltier module at its rated maximum current ($I_{max}$) is almost always thermally inefficient for precision cooling.

Our results demonstrate a critical divergence in thermoelectric performance: while cooling capacity ($Q_c$) scales by 16% per ampere, the hot-side heat load ($Q_h$) escalates by 37%. This asymmetry highlights a thermal runaway threshold beyond 5 A, where the Joule heating ($I^2R_e$) dominant regime risks exceeding the heat sink's dissipation capacity ($Q_h$ = 122 W). Consequently, we identify an optimal efficiency setpoint at ~1 A (COP = 3.1), suggesting that peak performance in real-world applications is achieved by minimizing current density rather than maximizing power input. Finally, the study proves that in 40 °C environments, the ambient thermal load shifts the $Q_c$ curve downward. This necessitates the use of multi-stage (cascaded) Peltier modules if sub-zero temperatures are required, as a single stage faces a diminishing return threshold earlier under high $T_{amb}$.

### *3.4. Python Implementation*

While the Simulink models rely on theoretical relationships, they often fail to account for contact resistance and non-linear parasitic losses in real-world packaging. This study introduces a hybrid empirical-computational framework that utilizes a dual-quadratic temperature evolution mapping to bridge the gap between ideal thermodynamics and practical implementation.

3.4.1. Temperature Evolution

Python results indicate that the temperature changes on both hot and cold sides follow a quadratic relationship with the temperature difference:

$$\Delta T_h = 0.0042983\Delta T^2 + 0.8250629\Delta T - 0.4188558 \quad (21)$$

$$\Delta T_c = -0.0042982\Delta T^2 - 0.1749429\Delta T - 0.4188338 \quad (22)$$

These equations represent both the initial rapid temperature change and the gradual approach to steady state, with the following key observations: nearly identical quadratic coefficients ($-0.0042983$ vs. $-0.0042982$) indicate symmetric thermal behavior, opposing linear terms (0.8250629 vs. $-0.1749429$) reflect the different heating/cooling dynamics and similar constant terms ($-0.4188558$ vs. $-0.4188338$) suggest consistent initial conditions.

Simulation at 5.0 A

The simulation at 5.0 A demonstrates the model's capability to predict Peltier module behavior at intermediate current levels. Considering an initial temperature (both sides) of 39.58 °C on both sides and a voltage of 9.85 V, the obtained results are shown in Table 5.

**Table 5.** Evolution of the temperature using Python simulation at an applied current of 5 A, 39.58 °C in both sides and a voltage of 9.85 V.

| ΔT (°C) | $T_h$ (°C) | $T_c$ (°C) | Voltage (V) |
|---|---|---|---|
| 0 | 39.58 | 39.58 | 9.85 |
| 5 | 43. 60 | 38.60 | 10.10 |
| 10 | 47.40 | 37.40 | 10.36 |
| 15 | 50.99 | 35.99 | 10.61 |
| 20 | 54.36 | 34.36 | 10.87 |

The simulation at 5.0 A confirms the model's robust interpolation capabilities, maintaining high physical fidelity across the non-linear transition between experimental data points. By preserving the linear voltage–temperature coupling and symmetric quadratic thermal gradients, the framework ensures a strict energy balance that aligns with both Seebeck effect predictions and internal Joule heating distributions. This alignment produces physically consistent steady-state conditions and realistic thermal response times, bridging the gap between theoretical heat transfer characteristics and practical thermoelectric behavior. Consequently, this lightweight Python implementation functions as a high-precision design tool, enabling the optimization of cooling strategies and the development of advanced pulse-width modulation (PWM) control logic for real-time thermal management in sensitive applications like PCR cycling or optoelectronics.

While the Simulink model provides a vital foundational understanding of thermoelectric theory, it operates under the assumption of ideal material properties and perfect thermal contact. In contrast, the Python-based empirical framework accounts for the inherent non-linearities of the physical assembly. The Simulink approach requires a deep set of manufacturer-specific constants, many of which, such as the internal thermal conductivity ($\kappa$) and electrical resistivity ($\rho$), are temperature-dependent and often unavailable for commercial-off-the-shelf (COTS) modules. The empirical model bypasses this black-box limitation by utilizing a voltage–temperature (V-ΔT) coupling coefficient. This allows for high-precision modeling ($R^2 > 0.98$) without the need for destructive testing to determine internal material variables.

A significant finding of this study is the near-identical quadratic coefficients for both the hot ($\Delta T_h$) and cold ($\Delta T_c$) side evolution equations. This symmetry reveals that the Joule heating contribution ($I^2R_e$) is the dominant factor in performance degradation at

higher currents, a phenomenon that Simulink often underestimates unless complex fluid-dynamic boundary conditions are manually integrated. By capturing this via regression, the proposed model inherently includes the parasitic heat loads that lead to the heat-dominant regime observed beyond 5 A. The transition from a solver-based environment (Simulink) to a functional programming environment (Python) facilitates the integration of Advanced Control Strategies. While Simulink is superior for initial design optimization and steady-state analysis, the Python implementation is optimized for active thermal management. Its lightweight O (1) computation of temperature setpoints makes it an ideal candidate for integration into microcontrollers managing PCR thermal cyclers, where rapid PWM adjustments are required to maintain a COP of 3.1 amidst fluctuating ambient loads.

It is important to clarify that pointing out how these results can be integrated into industrial or commercial facilities is not meant to promote a commercial application. Instead, it serves as direct proof of the framework's mathematical efficiency. Moving from a solver-dependent environment like Simulink to an open-source, functional programming platform like Python drastically reduces computational overhead. Because this empirical Python model relies on a high-precision voltage–temperature (V-ΔT) coupling coefficient rather than multi-layered, iterative loops, it achieves streamlined $O(1)$ computation time. This lightweight mathematical structure is a key novelty of this work. It makes the code uniquely suited for direct embedding into real-time microcontrollers for active thermal management, such as driving rapid pulse-width modulation adjustments to counter fluctuating ambient loads. The potential for its industrial application is simply a practical byproduct of the scientific optimization achieved in this study.

It is important to mention that the reported prediction errors were evaluated using a rigorous independent validation protocol. The dual-quadratic empirical equations were calibrated using 70% of the experimental dataset, while the remaining 30% was withheld from the training process and used exclusively for model validation. The reported errors (~0.14%) for the maximum temperature differential and =0.011% for the hot- and cold-junction temperature predictions, represent true out-of-sample performance rather than fitting accuracy. Thus, the reported data were accepted when $R^2 > 0.98$ in order to assure agreement between predictions and experimental observations.

Concerning computational efficiency, the proposed approach differs fundamentally from conventional finite-difference, finite-element, or SPICE-based thermoelectric simulations, which typically require iterative numerical solution procedures and repeated convergence calculations. In contrast, the present framework employs closed-form analytical expressions derived from the Laplace-domain transfer-function formulation (Equations (13) and (14)), coupled with algebraic dual-quadratic regression equations obtained from experimental data. Because the prediction of system states is performed through direct analytical evaluation rather than iterative numerical solving, the computational cost for each prediction remains effectively constant with respect to the model size, resulting in an O(1) computational complexity. This reduced computational load makes the proposed methodology particularly suitable for embedded and real-time applications, where computational resources are limited. In this way, the model can be executed using low-cost microcontrollers and integrated into active thermal-management systems employing pulse-width modulation control strategies, thereby enabling real-time temperature prediction and control without the overhead associated with conventional numerical solvers.

### *3.5. Pedagogical Integration and Virtual Laboratory Deployment*

The findings of this study demonstrate the potential of a dual-platform modeling approach as an effective pedagogical framework for teaching multiphysics coupling phe-

nomena, including thermoelectricity, electronics and heat transfer. By comparing a top-down, solver-based environment (MATLAB/Simulink) with a lightweight, open-source programming platform (Python), students can develop a deeper understanding of the complementary roles of theoretical modeling and data-driven empirical analysis in engineering problem solving.

Furthermore, the Python-based empirical regression framework can serve as the foundation of a digital twin-oriented educational technology, enabling students to explore and validate non-linear real-world system behavior through statistical error assessment and machine learning methodologies. The implementation of a standard 70/30 training-validation data-splitting strategy provides an accessible introduction to model verification and predictive analytics without the need for costly experimental infrastructure.

The virtual laboratory in this work offers an open-source learning environment that strengthens computational literacy while fostering practical skills in simulation, model calibration and performance validation. Importantly, the framework has been piloted with mechatronics and thermal engineering courses at the National Polytechnique Institute (Instituto Politécnico Nacional, IPN), particularly at the engineering campus located in Hidalgo, Mexico. Preliminary educational experiences indicate that the platform can reduce barriers associated with commercial software licensing while promoting greater student engagement with computational modeling, reproducible research practices, and interdisciplinary engineering analysis.

## 4. Conclusions

This research successfully developed two complementary approaches to modeling Peltier module behavior: a theoretical Simulink model and an empirically based Python implementation. Both models provide valuable insights into thermoelectric behavior under different operating conditions, with each offering distinct advantages for specific applications.

The Simulink model provides a robust theoretical foundation, allowing for detailed analysis of module behavior under varying ambient temperatures and power supply conditions. Its predictions align well with manufacturer specifications and provide valuable insights into the fundamental physics of thermoelectric operation. This model's strength lies in its comprehensive inclusion of physical parameters and its ability to simulate complex thermal interactions. The main findings of this work can be summarized as follows:

Maximum efficiency is achieved at low current densities (~1 A with a COP of 3.1). For currents exceeding 3 A, the COP drops significantly below 0.5, as more electrical energy is converted into waste heat than effective cooling.

A critical divergence occurs at 5 A. Beyond this point, heat dissipation ($Q_h$) surges (e.g., reaching 122 W at 6 A) while cooling capacity ($Q_c$) begins to decline due to dominant Joule heating effects.

High ambient temperatures (40 °C) shift the cooling curve downward, necessitating higher power consumption to achieve desired cold-junction temperatures. This highlights the necessity of multi-stage (cascaded) modules for sub-zero cooling in hot environments.

The Simulink model excels in theoretical parameter optimization and steady-state analysis. In contrast, the Python implementation is superior for real-time active thermal management and practical performance prediction, accounting for contact resistance and non-linear parasitic losses with high precision ($R^2 > 0.98$).

Ultimately, these models demonstrate that effective heat sink design and strict current management are essential for preventing module failure and maintaining optimal performance in real-world applications. Future work could focus on extending these models to

account for thermal cycling effects, long-term performance degradation, and integration with smart control systems.

**Supplementary Materials:** The following supporting information can be downloaded at: https://www.mdpi.com/article/10.3390/asi9080168/s1, Mathematical Relationships and Data Analysis.

**Author Contributions:** Conceptualization, F.J.M.-R.; methodology, M.A.D.-C. and A.M.-G.; software, H.Y.Á.-O.; validation, F.J.M.-R.; formal analysis, A.M.T.-H. and A.M.-G.; investigation, M.A.D.-C.; resources, F.J.M.-R.; data curation, H.Y.Á.-O.; writing—original draft preparation, F.J.M.-R.; writing—review and editing:, M.A.D.-C., A.M.-G. and A.M.T.-H.; visualization, A.M.T.-H. and A.M.-G.; supervision; project administration, M.A.D.-C.; funding acquisition, F.J.M.-R. All authors have read and agreed to the published version of the manuscript.

**Funding:** This research was funded by the Ministry of Science, Technology and Innovation of Mexico, projects numbers 232335, 241894, and 253178 of the Incentive Program for Research (PEI).

**Institutional Review Board Statement:** Not applicable.

**Informed Consent Statement:** Not applicable.

**Data Availability Statement:** The raw data supporting the conclusions of this article will be made available by the authors on request.

**Acknowledgments:** Authors thanks National Council for Science and Technology, México (CONACYT) for grant and scholarships.

**Conflicts of Interest:** The authors declare no conflicts of interest.

## Nomenclature

| | |
|---|---|
| $\Delta T$ | Temperature difference ($T_h - T_c$), °C |
| $\Delta T_{max}$ | Maximum temperature difference of the Peresistence Peltier module, K |
| $C$ | Thermal capacity, J/K |
| $c$ | Specific heat, kJ/kg K |
| $C_c$ | Cold-side thermal capacity, J/K |
| $C_h$ | Hot-side thermal capacity, J/K |
| COP | Coefficient of performance, % |
| $I$ | Electric current, A. |
| $I_{max}$ | Maximum electric current of the Peltier module, A. |
| $K_m$ | Thermal conductance of the Peltier module, W/K |
| $Q$ | Heat flux; heat absorption capacity W |
| $Q_c$ | Absorbed heat, W |
| $Q_{Fr}$ | Heat conduction by Fourier effect, W |
| $Q_h$ | Dissipated heat, W |
| $Q_J$ | Joule heating, W |
| $Q_{Pc}$ | Peltier Cooling, W |
| $Q_{Ph}$ | Peltier heating, W |
| $\delta$ | Density, kg/m$^3$ |
| $P_e$ | Electric power; power consumed W |
| $v$ | Heat sink volume, m$^3$ |
| $R$ | Electric resistance of the Peltier module, Ω |
| $R_c$ | Cold-side thermal resistance, K/W |
| $R_e$ | Internal electric resistance, Ω |
| $R_h$ | Hot-side thermal resistance, K/W |
| $R_p$ | Peltier module thermal resistance, K/W |
| $R_s$ | Silicone grease thermal resistance, K/W |
| $R_t$ | Thermal resistance, K/W |
| $s$ | Laplace variable |

| | |
|---|---|
| $S$ | Seebeck coefficient, V/K |
| $T$ | Temperature, °C |
| $\tau$ | Thomson coefficient |
| $T_a$ | Ambient temperature, °C |
| $T_c$ | Cold-side temperature, °C |
| $T_h$ | Hot-side temperature, °C |
| $V$ | Voltage, V |
| $V_{max}$ | Maximum voltage of the Peltier module |

## References


1. He, W.; Zhang, G.; Zhang, X.; Ji, J.; Li, G.; Zhao, X. Recent development and application of thermoelectric generator and cooler. *Appl. Energy* **2015**, *143*, 1–25. [CrossRef]
2. Hasan, M.; Zarin, N.A.; Ahmed, M.R.; Farrok, O. Global pathways for hybrid renewable energy systems: Challenges, solutions, policy, and regulatory frameworks. *Energy Convers. Manag. X* **2026**, *29*, 101534. [CrossRef]
3. Mahek, M.K.; Ramadan, M.; bin Dol, S.S.; Ghazal, M.; Alkhedher, M. A comprehensive review of thermoelectric cooling technologies for enhanced thermal management in lithium-ion battery systems. *Heliyon* **2024**, *10*, e40649. [CrossRef] [PubMed]
4. Shilpa, M.K.; Abdul Raheman, M.; Aabid, A.; Baig, M.; Veeresha, R.K.; Kudva, N. A Systematic Review of Thermoelectric Peltier Devices: Applications and Limitations. *Fluid Dyn. Mater. Process.* **2022**, *19*, 187–206. [CrossRef]
5. Riffat, S.B.; Ma, X. Thermoelectrics: A Review of Present and Potential Applications. *Appl. Therm. Eng.* **2003**, *23*, 913–935. [CrossRef]
6. Tian, Z.; Lee, S.; Chen, G. A Comprehensive Review of Heat Transfer in Thermoelectric Materials and Devices. *Annu. Rev. Heat Transf.* **2014**, *17*, 425–483. [CrossRef]
7. Laghzal, F.; Id Mbairi, S.; Tihane, A.; Alsaad, A.; Narjis, A. Comprehensive overview on thermoelectricity—Materials, applications and recent advances. *Mater. Sci. Eng. B* **2024**, *307*, 117512. [CrossRef]
8. Tritt, T.M. Thermoelectric Materials: Principles, Structure, Properties, and Applications. In *Encyclopedia of Materials: Science and Technology*; Elsevier: Amsterdam, The Netherlands, 2002; pp. 1–11. [CrossRef]
9. Dąbrowska, A.; Kobus, M.; Pękosławski, B.; Starzak, Ł. A Comparative Analysis of Thermoelectric Modules for the Purpose of Ensuring Thermal Comfort in Protective Clothing. *Appl. Sci.* **2021**, *11*, 8068. [CrossRef]
10. Rasoulpour, M.; Kouhikamali, R. Numerical simulation and parametric study of effective parameters in a thermoelectric dehumidifier with cooled plate using the Peltier effect. *Int. J. Thermofluids* **2026**, *33*, 101589. [CrossRef]
11. Alaoui, C. Peltier Thermoelectric Modules Modeling and Evaluation. *Chakib Alaoui Int. J. Eng.* **2011**, *5*, 2011–2114. Available online: https://www.researchgate.net/publication/228865590_Peltier_Thermoelectric_Modules_Modeling_and_Evaluation (accessed on 10 May 2025).
12. Guclu, T.; Cuce, E. Thermoelectric Coolers (TECs): From Theory to Practice. *J. Electron. Mater.* **2018**, *48*, 211. [CrossRef]
13. Boulgheb, A. Enhanced thermal management of SiGe HBT integrated circuits using the Peltier effect and DBC metal tracks. *Microelectron. Reliab.* **2025**, *174*, 115896. [CrossRef]
14. Samaš, V.; Gerlici, J. Electronic Regulation of Thermoelectric Modules in a Flow Cooler. *Transp. Res. Procedia* **2026**, *93*, 510–516. [CrossRef]
15. Afshari, F. Experimental Study for Comparing Heating and Cooling Performance of Thermoelectric Peltier. *J. Polytech.* **2020**, *23*, 889–894. [CrossRef]
16. Aridi, R.; Faraj, J.; Ali, S.; Lemenand, T.; Khaled, M. Thermoelectric Power Generators: State-of-the-Art, Heat Recovery Method, and Challenges. *Electricity* **2021**, *2*, 359–386. [CrossRef]
17. Enescu, D. Thermoelectric Energy Harvesting: Basic Principles and Applications. *Green Energy Adv.* **2019**, *1*, 38. [CrossRef]
18. Ha, J.; Kim, M.Y.; Park, S.J.; Jin, H. Realizing Seebeck-driven transverse thermoelectric generation in bulk composites. *Mater. Today Phys.* **2026**, *60*, 101976. [CrossRef]
19. Zhu, X.; Yu, Y.; Li, F. A review on thermoelectric energy harvesting from asphalt pavement: Configuration, performance and future. *Constr. Build. Mater.* **2019**, *228*, 116818. [CrossRef]
20. Tang, Z.; Guan, J.; Ke, S.; Gong, Q.; Jia, Y.; Liu, Q.; Liu, M.; Li, Y.; Cheng, F.; Wu, Y. Bioinspired water-driven ion reciprocating migration enables continuous power generation in cellulose-based ionic thermoelectrics. *Chem. Eng. J.* **2026**, *534*, 174810. [CrossRef]
21. Rolin, E.C.; Thomaz, G.R.; Moura, L.M. Energy efficiency of thermoelectric photovoltaic systems with thermoelectric cooling: A study based on numerical modeling and parameter identification. *Case Stud. Therm. Eng.* **2025**, *76*, 107410. [CrossRef]
22. Metallo, A. Numerical investigation of thermoelectric cooling for Li-ion battery modules: A high-efficiency, low-power approach. *Appl. Therm. Eng.* **2026**, *283*, 128979. [CrossRef]

23. Yang, H.; Zhu, Y.; Chong, H.M.H.; Huang, R. Accurate and efficient design and optimization of thermoelectric cooler via machine learning technologies. *Appl. Therm. Eng.* **2026**, *285*, 129224. [CrossRef]
24. Bun, K.; Rapaka, S.S.; Pathak, S.; Date, A.; Wang, X. Additive manufacturing, topology optimization of thermoelectric generators, and beyond: A comprehensive review on pioneering thermoelectric conversion for a sustainable future. *Appl. Therm. Eng.* **2025**, *278*, 127437. [CrossRef]
25. De Giuseppe, G.; Centuori, A.; Malvasi, A. An improved PZT cantilever SPICE model for practical energy harvesting circuits simulations and measurements. *Measurement* **2017**, *98*, 374–383. [CrossRef]
26. Aditya, K. A high-fidelity SPICE model of an Automotive DC actuator for predicting its performance with temperature. *Results Eng.* **2025**, *28*, 107831. [CrossRef]
27. Simsek, M.; Rahimi, J.; Aghakhani, A.; Basdogan, I. Nonlinear equivalent circuit modeling of bistable piezoelectric energy harvesters. *Int. J. Mech. Sci.* **2026**, *317*, 111510. [CrossRef]
28. Mahmood, H.A.; Jaddoa, A.A.; Al-Saadi, M.K. Improving the Performance of Thermoelectric Systems for Air Conditioning Using Different Configurations. *Front. Heat Mass Transf.* **2025**, *23*, 1281–1302. [CrossRef]
29. Lis, S.; Knaga, J.; Kurpaska, S.; Famielec, S.; Łyszczarz, P.; Machaczka, M. Optimizing Energy Efficiency in a Peltier-Module-Based Cooling Microunit through Selected Control Algorithms. *Energies* **2024**, *17*, 5031. [CrossRef]
30. Elnaggar, A.E.M.; Sharaf, S.; Abedel Rehim, Z.S.; El-Bayoumi, M.A.; Mustafa, H.M.M.; El Zoghby, H.M. Optimizing COP by RSM and MATLAB model of mini refrigerator based on thermoelectric units driven by solar photovoltaic. *Sci. Rep.* **2024**, *14*, 22766. [CrossRef] [PubMed]
31. Kobbekaduwa, K.P.V.B.; Subasinghe, N.D. Modelling and Analysis of Thermoelectric Generation of Materials Using Matlab/Simulink. *Int. J. Energy Power Eng.* **2016**, *5*, 97–104. [CrossRef]
32. Krismadinata; Rahim, N.A.; Ping, H.W.; Selvaraj, J. Photovoltaic Module Modeling using Simulink/Matlab. *Procedia Environ. Sci.* **2013**, *17*, 537–546. [CrossRef]
33. Tsai, H.-L.; Ci-Siang, T.; Yi-Jie, S. Development of generalized photovoltaic model using MATLAB/SIMULINK. In *Lecture Notes in Engineering and Computer Science*; Newswood Limited: Hong Kong, China, 2008; Volume 2173.
34. Tsai, H.-L.; Lin, J.-M. Model Building and Simulation of Thermoelectric Module Using Matlab/Simulink. *J. Electron. Mater.* **2010**, *39*, 2105–2111. [CrossRef]
35. Abdalla, A.; Islam, M.D.; Janajreh, I. Performance assessment of thermoelectric cooling for domestic air conditioning: Experimental and numerical study. *Int. Commun. Heat Mass Transf.* **2025**, *169*, 109954. [CrossRef]
36. Sirapani, D.; Ramadevi, C.; Revathi, J.; Rithanya, K.R.; Shakti, P. A Dual-Mode Peltier-based Thermal Management System with TEG Waste Heat Recovery and $I^2C$ Temperature Monitoring for Portable Applications. In *2025 3rd International Conference on Intelligent Cyber Physical Systems and Internet of Things (ICoICI)*; IEEE: New York, NY, USA, 2025; pp. 746–752. [CrossRef]
37. Russel, K.; Ewing, D.; Ching, C.Y. Characterization of a thermoelectric cooler based thermal management system under different operating conditions. *Appl. Therm. Eng.* **2013**, *50*, 652–659. [CrossRef]
38. Win, S.L.; Chiang, Y.-C.; Huang, T.-L.; Lai, C.-M. Thermoelectric Generator Applications in Buildings: A Review. *Sustainability* **2024**, *16*, 7585. [CrossRef]
39. Singh, R.; Dogra, S.; Dixit, S.; Vatin, N.I.; Bhardwaj, R.; Sundramoorthy, A.K.; Perera, H.C.S.; Patole, S.P.; Mishra, R.K.; Arya, S. Advancements in thermoelectric materials for efficient waste heat recovery and renewable energy generation. *Hybrid Adv.* **2024**, *5*, 100176. [CrossRef]
40. Goupil, C.; Seifert, W.; Zabrocki, K.; Müller, E.; Snyder, G.J. Thermodynamics of Thermoelectric Phenomena and Applications. *Entropy* **2011**, *13*, 1481–1517. [CrossRef]
41. Lineykin, S.; Ben-Yaakov, S. Modeling and analysis of thermoelectric modules. *IEEE Trans. Ind. Appl.* **2007**, *43*, 505–512. [CrossRef]
42. Chen, Z.; Shi, J.; Li, Y.; Ma, B.; Yan, X.; Liu, M.; Jin, H.; Li, D.; Jing, D.; Guo, L. Recent progress of energy harvesting and conversion coupled with atmospheric water gathering. *Energy Convers. Manag.* **2021**, *246*, 114668. [CrossRef]
43. Capolupo, F.; Strazzullo, P.; D'Alessandro, C.; Musto, M.; Russo, R. High-vacuum measuring system for accurate characterization of thermoelectric cooling modules. *Appl. Therm. Eng.* **2025**, *279*, 127615. [CrossRef]
44. Gámez-Avilez, J.D.; Islas-Pereda, S.; Velázquez-Limón, N.; Aguilar-Jiménez, J.A.; López-Martínez, L.A. Advances in Thermoelectric Generators Modules (TEGs): Applications, Performance, and Global Trends in Renewable Energy Systems. *Processes* **2026**, *14*, 901. [CrossRef]
45. Morese, S.; Nalli, K.P.; Pelz, U.; Subhash, S.K.; Kundu, S.; Goldschmidtböing, F.; Woias, P. A novel miniaturized paraffin actuator with Peltier-controlled cooling and graphene thermal conductivity enhancers. *Sens. Actuators A Phys.* **2026**, *399*, 117482. [CrossRef]
46. Riffat, S.B.; Ma, X. Improving the coefficient of performance of thermoelectric cooling systems: A review. *Int. J. Energy Res.* **2004**, *28*, 753–768. [CrossRef]
47. Mitrani, D.; Salazar, J.; Turó, A.; García, M.J.; Chávez, J.A. One-dimensional modeling of TE devices considering temperature-dependent parameters using SPICE. *Microelectron. J.* **2009**, *40*, 1398–1405. [CrossRef]
48. Ioffe, A.F. *Semiconductor Thermoelements, and Thermoelectric Cooling*; Infosearch, Ltd.: Chennai, India, 1957.

49. Zhang, H.Y.; Mui, Y.C.; Tarin, M. Analysis of thermoelectric cooler performance for high power electronic packages. *Appl. Therm. Eng.* **2010**, *30*, 561–568. [CrossRef]
50. Mannella, G.A.; La Carrubba, V.; Brucato, V. Peltier cells as temperature control elements: Experimental characterization and modeling. *Appl. Therm. Eng.* **2014**, *63*, 234–245. [CrossRef]
51. Ogata, K. *Ingeniería de Control Moderna*; Prentice Hall Hispanoamericana, S.A.: Mexico City, Mexico, 1998.
52. Gobpant, J.; Sakulkalavek, A.; Sriniratkul, P.; Sa-I, S.; Rudradawong, C.; Tian, J.; Nguyen, V.Q.; Ono, T.; Van Toan, N. Flexible thermoelectric cooler with optimized fill factor and radiative cooling integration for energy-efficient wearable thermal management. *Sustain. Mater. Technol.* **2025**, *46*, e01742. [CrossRef]
53. Félix-Herrán, L.C.; García-Juárez, A.; García-Delgado, L.A.; González-Aguayo, P.S.; Lozoya-Santos, J.d.-J.; Noriega, J.R. Characterization System for Heat-Energy to Electric-Energy Conversion from Concrete by Means of a Thermoelectric Module. *Sensors* **2022**, *22*, 1881. [CrossRef] [PubMed]
54. Kumar, V.; Shakher, C. Qualitative and quantitative investigations of temperature distribution, heat flow, and heat transfer parameters from the heated objects using lensless Fourier transform digital holography: A review. *Opt. Laser Technol.* **2024**, *168*, 109918. [CrossRef]
55. Lertlam, K.; Phosing, T.; Salim, M.A.; Photong, C. Simplified semiclassical dicke quantum battery with MATLAB/simulink model. *Results Eng.* **2026**, *30*, 110499. [CrossRef]
56. Kalay, A.; Kapucu, C. Integrating NeuralProphet (NP) forecasting with MATLAB/simulink for energy-efficient PV-grid water pumping. *Energy Rep.* **2026**, *15*, 109227. [CrossRef]
57. Khoshraftar, Z.; Yazdi, M.S.K.; Mosavi, M.R.; Ghaemi, A. Chapter 2—MATLAB and python functions of neural networks. In *Artificial Neural Networks in Chemical Engineering Processes*; Elsevier: Amsterdam, The Netherlands, 2026; pp. 37–87. [CrossRef]
58. Kryotherm. Available online: http://www.kryotherm.ru (accessed on 5 April 2023).
59. Beijing Huimao Cooling Equipment. Available online: http://www.huimao.com (accessed on 5 April 2024).
60. II-VI Marlow. Available online: https://www.coherent.com/content/dam/coherent/site/en/resources/datasheet/materials/related-resources/thermoelectrics/thermoelectric-coolers-space-qualification-process.pdf (accessed on 6 June 2025).
61. Hi-Z Technology. Available online: http://hi-z.com (accessed on 6 June 2025).
62. Lineykin, S.; Ben-Yaakov, S. Spice compatible equivalent circuit of the energy conversion processes in thermoelectric module. *IEEE Isr. Conv.* **2004**, *23*, 346–349. [CrossRef]
63. Wielgosz, S.E.; Clifford, C.E.; Yu, K.; Barry, M.M. Fully–coupled thermal–electric modeling of thermoelectric generators. *Energy* **2023**, *266*, 126324. [CrossRef]
64. Ramzy, K.; Abdelgaleel, M.; Alswat, M.; Kabeel, A.E.; Mosalam, H.; abdelAziz, E.A. Enhancing the performance of a solar distiller using phase change materials integrated with Peltier modules and Heaters: Energy, exergy, and economic analysis. *Appl. Therm. Eng.* **2025**, *274*, 126674. [CrossRef]
65. Atmanandmaya; Loganathan, U.; Subba Reddy, B. A novel approach to enhance the efficiency of decentralized thermal desalination system using Peltier modules. *Desalination* **2025**, *614*, 119127. [CrossRef]
66. Binninger, R.; Unmüßig, S.; Vergez, M.; Bartel, M.; Schäfer-Welsen, O. Customized measuring station for Peltier modules. *Heliyon* **2024**, *10*, e25743. [CrossRef] [PubMed]
67. Silva, D. Modeling the Transient Response of Thermal Circuits. *Appl. Sci.* **2022**, *12*, 12555. [CrossRef]
68. Hao, X.; Peng, B.; Xie, G.; Chen, Y. Efficient on-chip hotspot removal combined solution of thermoelectric cooler and mini-channel heat sink. *Appl. Therm. Eng.* **2016**, *100*, 170–178. [CrossRef]
69. Chang, Y.-W.; Chang, C.-C.; Ke, M.-T.; Chen, S.-L. Thermoelectric air-cooling module for electronic devices. *Appl. Therm. Eng.* **2009**, *29*, 2731–2737. [CrossRef]
70. Chein, R.; Chen, Y. Performances of thermoelectric cooler integrated with microchannel heat sinks. *Int. J. Refrig.* **2005**, *28*, 828–839. [CrossRef]
71. Huang, H.-S.; Weng, Y.-C.; Chang, Y.-W.; Chen, S.-L.; Ke, M.-T. Thermoelectric water-cooling device applied to electronic equipment. *Int. Commun. Heat Mass Transf.* **2010**, *37*, 140–146. [CrossRef]
72. Zhu, L.; Tan, H.; Yu, J. Analysis on optimal heat exchanger size of thermoelectric cooler for electronic cooling applications. *Energy Convers. Manag.* **2013**, *76*, 685–690. [CrossRef]


**Disclaimer/Publisher's Note:** The statements, opinions and data contained in all publications are solely those of the individual author(s) and contributor(s) and not of MDPI and/or the editor(s). MDPI and/or the editor(s) disclaim responsibility for any injury to people or property resulting from any ideas, methods, instructions or products referred to in the content.